Ion and Electron Dynamics in Nonlinear PIC Simulations

S. Jolliet*, A. Bottino†, P. Angelino*, T. M. Tran*, B. F. McMillan*, R. Hatzky**, A. G. Peeters†, E. Poli†, O. Sauter* and L. Villard*

* *Ecole Polytechnique Fédérale de Lausanne*
Centre de Recherches en Physique des Plasmas
Association Euratom-Confédération Suisse
CH-1015 Lausanne, Switzerland
† *Max Planck Institut für Plasmaphysik*
IPP-EURATOM Association
Garching, Germany
** *Computer Center of the Max-Planck-Gesellschaft*
D 85748 Garching, Germany

Abstract. ITG and ETG turbulence is investigated with the nonlinear global PIC code ORB5. The large variety of numerical schemes and simulations domains used has sometimes lead to important discrepancies in the transport predictions. In order to discuss these disagreements, emphasis must be put on ways to check the numerical accuracy, such as energy conservation and numerical noise measurement. This paper therefore presents benchmarks, new algorithms and a noise diagnostic [1]. After having demonstrated the numerical quality of our simulations, 2 topics are visited: the unclear role of the parallel nonlinearity [4, 5] and the transport level in ETG turbulence, for which predictions differing by one order of magnitude had been made elsewhere [2, 3].

Keywords: gyrokinetics, PIC, microinstabilities, zonal flows, ETG
PACS: 52.30.Gz,52.35.Qz,52.35.Ra

INTRODUCTION

Gyrokinetic codes are powerful tools for studying microinstabilities, which are commonly held responsible for anomalous transport. Several numerical schemes are employed. In Eulerian codes, the distribution function is discretized on a 5D grid and is evolved with finite difference or spectral methods. Semi-Lagrangian codes use the same discretization, but the temporal evolution is done by tracing back in time the trajectories ending up at grid points at each time step. In Particle-In-Cell (PIC) codes, the distribution function is discretized with markers. Besides, microinstabilities can be simulated locally (along a field-line), globally (in a full torus) or with flux-tube (in a tube surrounding the field-line). These various types of numerical schemes and geometrical domains can lead to important discrepancies in the predicted radial transport coefficients. For example, flux-tube simulations [2] and global PIC simulations [3] give transport coefficients that differ by 1 order of magnitude for ETG turbulence. Moreover, the role of the parallel nonlinearity (PNL) is still controversial [4, 5]. In order to understand the origin of these discrepancies, it is important to benchmark gyrokinetic codes and to provide diagnostics that show the numerical quality of simulations. The numerical noise associated with the PIC method inevitably leads to the loss of energy conservation in the late nonlin-

ear phase. In the case of ETG simulations, the turbulence dies away at late times due to discrete particles noise [7], yielding a unphysical transport level. This motivates us to develop the global nonlinear PIC code ORB5 [6] to obtain low-noise, energy and particle number conserving simulations: In this paper, we will focus on demonstrating the convergence of our simulations. Several new algorithms will be presented, which strongly improve the quality of our simulations, together with a huge decrease of CPU. Finally, we will investigate 2 important issues, namely the role of the PNL in ITG turbulence and the influence of numerical noise on ETG turbulence.

THE GYROKINETIC MODEL

We consider gyrokinetic equations of Hahm [8] with the following gyrokinetic ordering:

$$\frac{\omega}{\Omega_i} \sim \frac{k_\parallel}{k_\perp} \sim \frac{e\phi}{T_e} \sim \frac{\rho_{L,i}}{L_n} \sim \frac{\rho_{L,i}}{L_{T,i}} \sim \frac{\rho_{L,i}}{L_{T,e}} \sim \varepsilon_g, \qquad \frac{\rho_{L,i}}{L_B} \sim \varepsilon_B, \tag{1}$$

ω and Ω_i are characteristic fluctuation and cyclotron frequencies, $k_\parallel$ and $k_\perp$ are the parallel and perpendicular components of the wave number with respect to the magnetic field, ϕ is the fluctuating electrostatic potential, $\rho_{L,i}$ is the Larmor radius, $L_n, L_{T,i}, L_{T,e}$ and L_B are characteristic lengths for density, ion and electron temperature and magnetic field. The 2 small parameters are such that $\varepsilon_g \sim \rho^*$ and $\frac{\varepsilon_g}{\varepsilon_B} \sim \varepsilon_a^{-1} \gg 1$, where $\rho^* = \frac{\rho_{L,i}}{a}$, a is the Tokamak minor radius, and $\varepsilon_a = \frac{a}{R_0}$ is the inverse aspect ratio, R_0 being the major radius. Terms of order $\mathscr{O}(\varepsilon_B^2)$ are neglected. Equations of motion are:

$$\frac{\mathrm{d}\vec{R}}{\mathrm{d}t} = \underbrace{v_\parallel \vec{h}}_{\mathscr{O}(1)} + \underbrace{\frac{1}{\Omega_i B_\parallel^*}\left(v_\parallel^2 + \frac{v_\perp^2}{2}\right)\left(\vec{h}\wedge\vec{\nabla}B\right) - \frac{v_\parallel^2}{\Omega_i B_\parallel^*}\vec{h}\wedge\left[\vec{h}\wedge(\vec{\nabla}\wedge\vec{B})\right]}_{\mathscr{O}(\varepsilon_B)} + \underbrace{\frac{\langle\vec{E}\rangle\wedge\vec{B}}{B_\parallel^* B}}_{\mathscr{O}(\varepsilon_g)} \tag{2}$$

$$\frac{\mathrm{d}v_\parallel}{\mathrm{d}t} = \underbrace{\frac{1}{2}v_\perp^2\vec{\nabla}\cdot\vec{h}}_{\mathscr{O}(\varepsilon_B)} + \underbrace{\frac{q_i}{m_i}\langle\vec{E}\rangle\cdot\vec{h}}_{\mathscr{O}(\varepsilon_g^2)} + \underbrace{\frac{v_\parallel}{BB_\parallel^*}\langle\vec{E}\rangle\cdot\left\{\left(\vec{h}\wedge\vec{\nabla}B\right) - \left(\vec{h}\wedge\left[\vec{h}\wedge\left(\vec{\nabla}\wedge\vec{B}\right)\right]\right)\right\}}_{\mathscr{O}(\varepsilon_g\varepsilon_B)} \tag{3}$$

$$\frac{\mathrm{d}\mu}{\mathrm{d}t} = 0 \tag{4}$$

where $\vec{h} = \frac{\vec{B}}{B}$, $\Omega_i = \frac{q_i B}{m_i}$, $B_\parallel^* = B + \frac{m_i v_\parallel}{q_i}\left(\vec{\nabla}\times\vec{h}\right)\cdot\vec{h}$, $\mu = \frac{v_\perp^2}{2B}$ is the magnetic moment and $\langle\vec{E}\rangle$ is the gyro-averaged electric field. These equations include the parallel motion, drifts due to the magnetic field gradient and its curvature, the pressure gradient and the perturbed electric field. The equation for the parallel velocity contains a mirror term to account for trapped particles and the so-called *parallel nonlinearity*. Since it is a second order term, many gyrokinetic models ignore it.

To solve the Vlasov equation, a δf scheme [9] is applied, in other words the distribution function f is split into an equilibrium part f_0 (in our case a Maxwellian) and a perturbed

part δf:

$$f(\vec{R},v_\parallel,\mu,t) = f_0(\varepsilon,\mu,\Upsilon)+\delta f(\vec{R},v_\parallel,\mu,t) \quad (5)$$

$$f_0(\varepsilon,\mu,\Upsilon) = \frac{n_0(\Upsilon)}{(2\pi)^{3/2}v_{thi}^3(\Upsilon)}\exp\left(-\frac{\varepsilon}{T_i(\Upsilon)}\right) \quad (6)$$

ε is the kinetic energy of a single particle, $\varepsilon=\frac{1}{2}mv^2$, n_0 is the equilibrium density and v_{thi} the ion thermal speed. 3 different coordinates can be chosen for Υ. If $\Upsilon=\psi$, where ψ is the poloidal flux, the resulting *local* Maxwellian can lead to the generation of spurious zonal flows, as shown in [10], since $\left.\frac{\mathrm{d}f_0}{\mathrm{d}t}\right|_0 \sim \left.\frac{\mathrm{d}\psi}{\mathrm{d}t}\right|_0 \neq 0$ (the subscript 0 means "along the unperturbed orbits"). The latter can be avoided by using a *canonical* Maxwellian, i.e. $\Upsilon=\psi_0$, where $\psi_0=\psi+\frac{q_i}{m_i}\frac{F(\psi)}{B}v_\parallel$ is the toroidal angular momentum. The canonical Maxwellian can be corrected by using $\hat{\psi}$ instead of ψ_0, where $\hat{\psi}=\psi_0-\mathrm{sign}(v_\parallel(t_0))\frac{q_i}{m_i}R_0\sqrt{2(\varepsilon-\mu B_0)}\mathscr{H}(\varepsilon-\mu B_0)$ is another constant of motion defined only for passing particles due to the Heavyside function $\mathscr{H}(x)$. $\hat{\psi}$ can be viewed as the closest constant of motion to ψ. The Vlasov equation then reads $\frac{\mathrm{d}\delta f(\vec{R},v_\parallel,\mu,t)}{\mathrm{d}t}=\tau(\vec{E})$, where

$$\tau(\vec{E}) = -\,f_0(\Upsilon,v_\parallel,\mu)\kappa(\Upsilon)\left(\left.\frac{\mathrm{d}\Upsilon}{\mathrm{d}t}\right|_0+\left.\frac{\mathrm{d}\Upsilon}{\mathrm{d}t}\right|_1\right)+\frac{q_i f_0(\Upsilon,v_\parallel,\mu)}{T(\Upsilon)}\langle\vec{E}\rangle\cdot\left.\frac{\mathrm{d}\vec{R}}{\mathrm{d}t}\right|_0 \quad (7)$$

and $\kappa(\upsilon)=\frac{\mathrm{dln}\,f_0(\Upsilon,v_\parallel,\mu)}{\mathrm{d}\Upsilon}$. The subscript 1 refers to terms containing the gyro-averaged electric field. The model is closed with a linearized Poisson equation, which can be reduced to a quasineutrality condition. Furthermore assuming $k_\perp\rho_{L,i}\ll 1$ (long-wavelength approximation) and adiabatic electrons on magnetic surfaces, it is written as:

$$\frac{n_0(\psi)}{Z_iT_e(\psi)}\left(\phi(\vec{x},t)-\bar{\phi}(\psi,t)\right)-\vec{\nabla}_\perp\cdot\left(\frac{Z_in_0(\psi)}{B\Omega_i}\vec{\nabla}_\perp\phi(\vec{x},t)\right)=Z_i\delta n_i \quad (8)$$

Where a term of order $\mathscr{O}(\varepsilon_g^2)$ has been neglected. The first term of the LHS is the adiabatic contribution. The so called *zonal flow* term is described with the flux-surface averaged potential:

$$\bar{\phi}(\psi,t)=\frac{\int\phi(\psi,\theta,\varphi,t)J_{\psi\theta\varphi}(\psi,\theta)d\theta d\varphi}{\int J_{\psi\theta\varphi}(\psi,\theta)d\theta d\varphi} \quad (9)$$

Where $J_{\psi\theta\varphi}(\psi,\theta)$ is the Jacobian for (ψ,θ,φ). The second term is the polarization density, and the RHS is the perturbed density whose computation is called the *charge assignment*:

$$\delta n_i=\int B_\parallel^* d\vec{R}dv_\parallel d\mu d\alpha\,\delta f(\vec{R},v_\parallel,\mu,t)\delta(\vec{R}+\vec{\rho}_{L,i}-\vec{x}) \quad (10)$$

α is the gyro-angle. The great advantage of Hahm's equations lies in its associated conservation laws. The total number of particles is conserved: $\frac{\mathrm{d}N_{ph}}{\mathrm{d}t} = 0$, with:

$$\frac{\mathrm{d}N_{ph}}{\mathrm{d}t} = \frac{\mathrm{d}}{\mathrm{d}t}\int f B_{\|}^{*} d\vec{R} dv_{\|} d\mu d\alpha = 0. \tag{11}$$

If one defines the total kinetic and potential energy of the system:

$$E_{kin} = \int m_i \left(\mu B + \frac{v_{\|}^2}{2}\right) f B_{\|}^{*} d\vec{R} dv_{\|} d\mu d\alpha \tag{12}$$

$$E_f = \frac{q_i}{2}\int d\vec{x}\big(\langle n_i\rangle(\vec{x},t) - n_0(\Upsilon)\big)\phi(\vec{x},t). \tag{13}$$

Then the total energy is conserved, i.e. $\frac{\mathrm{d}E_{kin}+E_f}{\mathrm{d}t} = 0$. The proof can be found in [11]. Such conservation laws provide a useful check of the quality of the simulation at each time step. Finally, due to the absence of external sources in our model, the free evolving temperature and density profiles relax during the nonlinear phase.

NUMERICAL IMPLEMENTATION

δf is discretized according to the PIC method:

$$\delta f = \frac{N_{ph}}{N}\sum_{p=1}^{N}\frac{1}{2\pi B_{\|}^{*}} w_p(t)\delta\big(\vec{R}-\vec{R}_p(t)\big)\delta\big(v_{\|}-v_{\|,p}(t)\big)\delta\big(\mu-\mu_p(t_0)\big) \tag{14}$$

It is therefore described with N markers, evolving in the 5D phase space and carrying a weight w. Vlasov equation can be solved with the *standard-*δf scheme by a temporal integration of Eq. (7), or with the *direct-*δf scheme. The latter uses the conservation of f in the phase space, so we simply have $\delta f = f(t_0) - f_0\big(\vec{R}(t), v_{\|}(t), \mu(t_0)\big)$. Equations of motion are either solved in cartesian coordinates (r,φ,z) or in "pseudo-cartesian" coordinates $(\xi = s\cos\theta_*, \varphi, \eta = s\sin\theta_*)$, where $s = \sqrt{\psi/\psi_{\mathrm{edge}}}$ is the magnetic label and $\theta_* = \frac{1}{q(\psi)}\int_0^{\theta}\frac{\vec{B}\cdot\vec{\nabla}\varphi}{\vec{B}\cdot\vec{\nabla}\theta'}d\theta'$ is the straight-field-line angle. The use of (ξ,η) avoids the singularity on axis. Poisson equation is solved on a (s,θ,φ) or (s,θ_*,φ) grid with 3D cubic B-spline finite elements [12]. The second option avoids interpolations $(r,z)\rightarrow(s,\theta/\theta_*)$ during the charge assignment and the electric field computation. Depending on the processor architecture, the total CPU gain can be as high as 25%.
Numerical noise is produced during the charge assignment, where each marker is represented by a gyro-ring projected onto a discrete grid. A common way to reduce the numerical noise is to Fourier-filter the perturbed density:

$$F\delta n(\vec{x},t) = \sum_{m,n} f_{m,n}(s)\widehat{\delta n}_{m,n}(s,t)\, e^{im\theta_*}\, e^{in\varphi} \tag{15}$$

A first naive choice for $f_{m,n}(s)$ is called the *square* filter (SF): all modes outside a window $[m_{\max} : m_{\min}]\times[n_{\max} : n_{\min}]$ are suppressed after the charge assignment. However,

this type of filter contains modes that are inconsistent with the gyrokinetic ordering (1). Assuming a (m,n) mode is propagating locally at $s = s_0$, as $k_\parallel = \frac{m+nq(s)}{q(s)r}$, the highest $k_\parallel$ mode contained in the SF will be $k_\parallel^{\max} \cong \frac{2m_{\max}}{q(s_0)R_0}$. Approximating $k_\perp \sim \frac{m}{\rho}$, we get:

$$\left(\frac{k_\parallel}{k_\perp}\right)^{\max} \cong \frac{\varepsilon_a}{q(s_0)} \cong 0.26 \gg \rho^* \tag{16}$$

with the CYCLONE base case parameters [13]. Obviously, this simple local estimate shows that (16) breaks the gyrokinetic ordering (1), independently of the plasma size. Consequently a SF contains unphysical high $k_\parallel$ modes, which increases numerical noise. A better choice is called the *field-aligned* filter (FAF). For each n in $[n_{\max} : n_{\min}]$, the modes $[-nq(s) - \Delta m : -nq(s) + \Delta m]$ are retained. Δm can be estimated from an ITG dispersion relation [14]:

$$\Delta m \cong \frac{q(s_0)}{2}\sqrt{\left(1 - \frac{2}{\eta_i}\right)}\frac{R_0}{L_{T,i}} \tag{17}$$

Where $\eta_i = \frac{L_n}{L_{T,i}}$. Note that Δm only depends on the profile gradients. We obtain:

$$\left(\frac{k_\parallel}{k_\perp}\right)^{\max} \cong \frac{1}{2}\sqrt{\left(1 - \frac{2}{\eta_i}\right)}\frac{\rho_{L,i}}{L_{T,i}} \sim \frac{1}{2}\sqrt{\left(1 - \frac{2}{\eta_i}\right)}\rho^* \tag{18}$$

As a result the FAF is consistent with the gyrokinetic ordering (1), since it keeps the field aligned structure of ITG modes. The time step of a simulation is closely linked with the Fourier filter. The general time step criterion writes:

$$\omega \delta t = \delta \ll 1 \tag{19}$$

Where ω is the fastest relevant frequency of the system. For ITG turbulence in a tokamak, there are mainly 3 frequencies of interest: the transit frequency $\omega_t = \frac{v_\parallel}{q(s)r}$, the frequency related to the $\vec{E} \times \vec{B}$ velocity $\omega_{\vec{E}\times\vec{B}} = k_\perp v_{\vec{E}\times\vec{B}} \cong M k_\perp v_{thi}$, where M is the Mach number and the Landau damping frequency $\omega_\parallel = k_\parallel v_\parallel$. Using previous estimates of $k_\parallel$ for both kinds of filter, the time step criterion for $\omega_\parallel$ becomes:

$$\Delta t_\parallel^s \Omega_i \cong \frac{\delta}{2}\frac{a}{\rho_0}\frac{1}{q(s_0)}\varepsilon_a \tag{20}$$

$$\Delta t_\parallel^{fa} \Omega_i \cong \frac{\delta\sqrt{\tau}}{a}\frac{2L_{T,i}}{\sqrt{1 - \frac{2}{\eta_i}}}(\rho^*)^{-1} \tag{21}$$

The $(\rho^*)^{-1}$ dependence of Eq. (21) clearly shows the beneficial influence of the FAF in the parallel direction. However, quantitative estimates of ω_t and $\omega_{\vec{E}\times\vec{B}}$ are needed to see if the FAF has an influence on the global time step of the simulation. Fig. 1 shows estimation of the different time steps for modes having the maximum $k_\parallel/k_\perp$ with the CYCLONE parameters and $M = 5 \cdot 10^{-3}$, which is the typical value observed in our

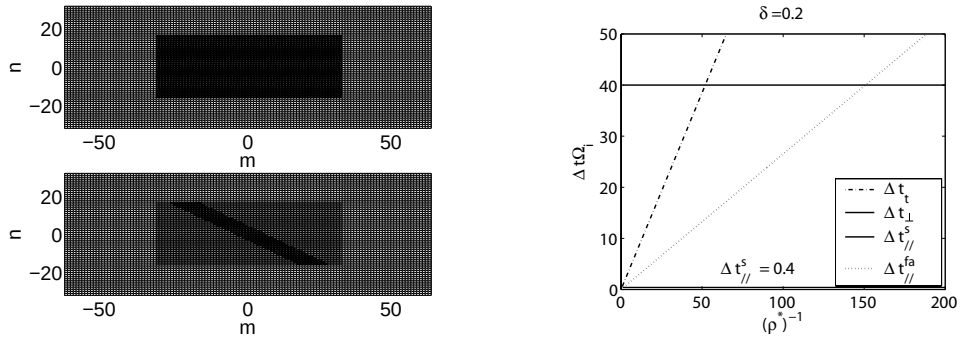

FIGURE 1. Left: square (top) and field-aligned (bottom) in (m,n) space. Right:time step criterion as a function of $(\rho^*)^{-1}$

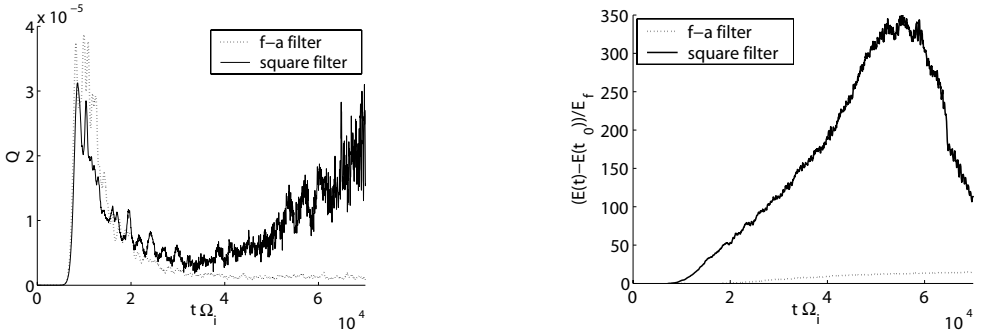

FIGURE 2. Average radial heatflux (left) and relative energy conservation (right) vs time for a square filter (solid line) and a field-aligned (dotted line) simulation

simulation. The value of $\Delta t^s_{\|}$ is extremely small. Since usual time steps are of the order of $5\Omega_i^{-1}$, we conclude that the evolution of many modes in the SF will be inaccurate and will impair the quality of the simulation. On the other hand, in the limit of small-ρ^* plasmas, simulation using a FAF could be run, according to our estimate, with a one order of magnitude higher time step, thus decreasing CPU by the same amount. In order to confirm our predictions, the FAF has been tested in a simulation with the following parameters: $\rho^* = \frac{1}{40}$,$R_0/L_{T,i} = 13$,$\eta_i = \infty$,$\varepsilon_a = 5$, $(m,n) \in [\pm 40, \pm 16]$, $\Delta m = 5$ and $\Delta t = 40\Omega_i^{-1}$. Convergence tests have been made to ensure that Δm is large enough. Note that using θ_* instead of θ as poloidal angle narrows the poloidal spectrum of all toroidal modes. Fig. 2 shows the temporal evolution of the volume-averaged radial heat flux Q, defined by:

$$Q = \sum_{p=1}^{N} w_p \frac{1}{2} m v_p^2 \, \frac{\langle \vec{E} \rangle \times \vec{B}}{B_{\|}^* B} \cdot \frac{\vec{\nabla}\psi}{|\vec{\nabla}\psi|} \Bigg|_{\vec{R}_p, v_{\|,p}, \mu_p} \tag{22}$$

The square filter simulation is totally unphysical. The system does not relax to a quasi-steady state. On the contrary, numerical noise totally kills the simulation. In the field-aligned case, the system relaxes to a quasi-steady state. The relative energy conservation is improved by one order of magnitude with the same number of markers. To get similar

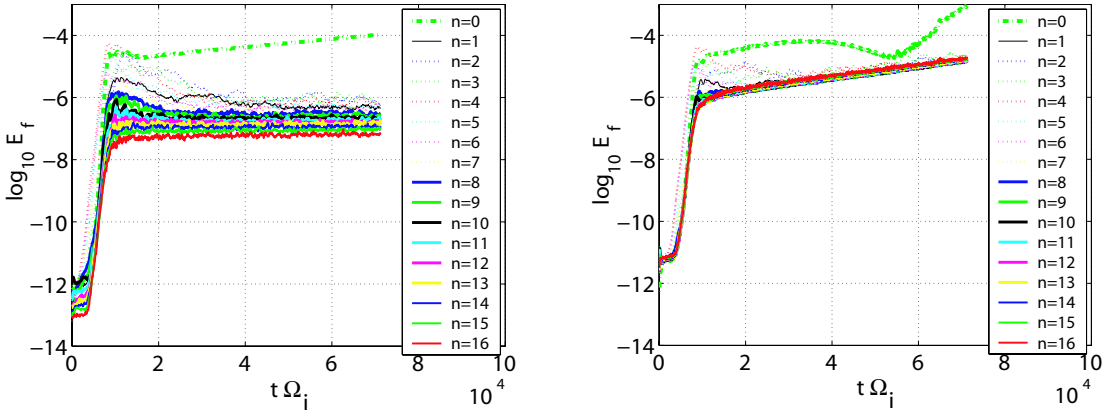

FIGURE 3. Energy of toroidal modes with the field-aligned (left) and square (right) filters. The $n = 0$ mode is the dashed-dotted line.

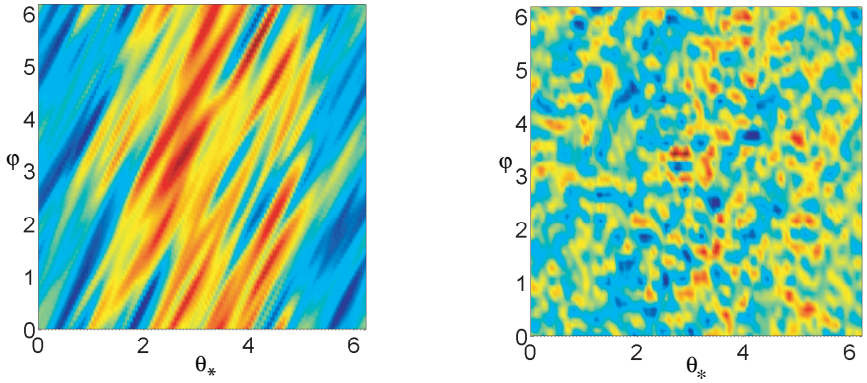

FIGURE 4. Late-time structure of potential along the magnetic field-line $s = 0.5$ for the field-aligned (left) and square (right) filters

results with a SF, many more markers and a smaller time step would be required. The degradation of the SF simulation can be seen on Fig. 3. The growth of the $n \neq 0$ modes at late times is due to high $k_{\|}$ modes, and is not observed for the field-aligned case. Finally, the late-time structure of the electric potential along the $s = 0.5$ field line is shown on Fig. 4. ITG modes tend to align with the field lines, but this feature is apparently destroyed with the SF: the perturbation is a superposition of high-$k_{\|}$ modes.

The notion of convergence is an important issue in nonlinear gyrokinetic simulations. Believable physical results require convergence in terms of grid resolution and time step, but a PIC simulation needs to be converged with respect to the number of markers as well. The left plot of Fig. 5 shows a scan for the number of markers. The overshoot is shifted in time as the number of markers is increased, and it becomes hard to say if the convergence is reached or not. This is because the initial level of the perturbation is inversely proportional to the number of markers: the initial weights are defined by:

$$w_p(t_0) = A_0 f_0(\vec{R}(t_0), v_{\|}(t_0), \mu(t_0))\Omega_p R_p \tag{23}$$

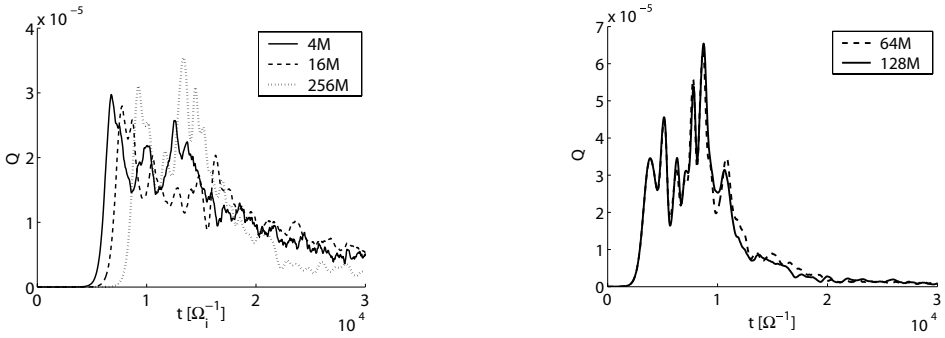

FIGURE 5. Temporal evolution of radial heat flux with a random initialization (left) and mode initialization (right) for different number of markers.

where A_0 is the initial amplitude of the perturbation, Ω_p is the volume of phase space occupied by the marker p and $R_p \in [-1:1]$ is a random number. Eq. (23) will be denoted as the *random* initialization. An alternative to Eq. 23 is obtained by defining initial weights by:

$$w_p(t_0) = A_0 f_0\big(\vec{R}(t_0), v_{\|}(t_0), \mu(t_0)\big)\Omega_p \cos(m_0\theta_*(t_0) - n_0\varphi(t_0))\frac{L_{T,i}(s_0)}{L_{T,i}(s(t_0))} \qquad (24)$$

Where m_0 and n_0 are integers. Eq. (24) will be denoted as the *mode* initialization. The right plot of Fig. 5 shows the radial heat flux of a simulation with the mode initialization for $N = 64 \cdot 10^6$ and $N = 128 \cdot 10^6$. Both curves are almost similar. We can therefore say that our simulation is converged. This is because the initial level of the perturbation obtained with the mode initialization does not depend on the number of markers anymore. Eq. (24) is useful to determine the convergence of a simulation with the number of markers. However, the mode initialization is not really physical, as one mode strongly dominates in the linear phase. This can lead to a different bursty transient phase. A more realistic method would be to initialize several modes instead of one. Nevertheless, the convergence in N does not depend on the initial conditions.

THE ROLE OF THE $\|$ NONLINEARITY

The role of the PNL is still unclear. PIC simulations in cylinder [15] and tokamak [4] geometry showed that this term has an effect on the zonal flow structure. On the other hand, other authors found that this term has no influence and transport for small-ρ^* plasmas [5]. CYCLONE simulations were performed with $\rho^* = 1/175$ and $\rho^* = 1/35$, with and without the PNL. On Fig. 6, one sees that if the PNL is not retained, energy conservation is totally lost, even for small ρ^*-plasmas. Still on Fig. 6, the temporal evolution of χ_i/χ_{GB} against $R_0/L_{T,i}$ is plotted, where:

$$\chi_i \equiv -\frac{Q}{n_i\vec{\nabla}T_i},\ \chi_{\mathrm{GB}} = \frac{\rho_{L,i}^2 v_{th,i}}{L_n} \qquad (25)$$

Both profiles are averaged over $s_0 \pm 0.05$. Globally, the evolution of χ_i/χ_{GB} and $R_0/L_{T,i}$

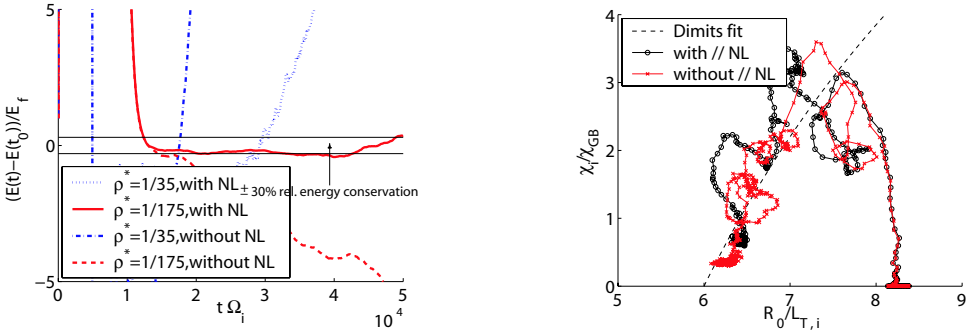

FIGURE 6. Relative energy conservation for CYCLONE simulations (left) and temporal evolution of χ_i/χ_{GB} vs $R_0/L_{T,i}$ (right). Profiles have been averaged between $s_0 \pm 0.05$.

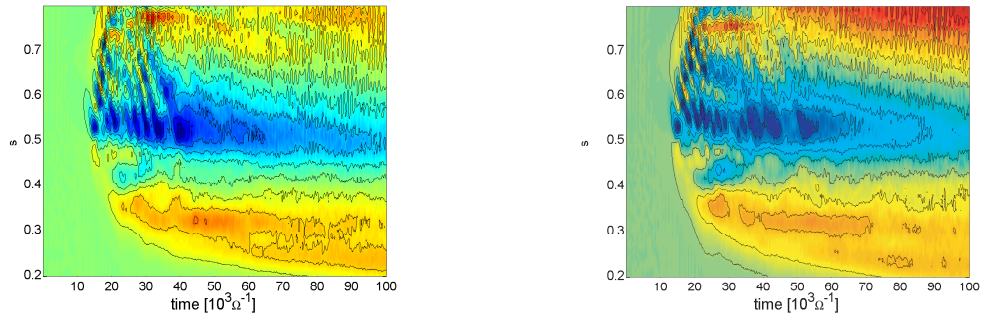

FIGURE 7. Temporal evolution of $\nabla\bar{\phi}(s)$ for CYCLONE simulations with (left) and without (right) PNL.

follows the Dimits fit, and there is no visible effect of the PNL on transport. Our simulations also show that the absence of the PNL does not induce any relevant global effect. On Fig. 7, the temporal evolution of $\nabla\bar{\phi}(\psi,t)$ is shown for cases with and without the PNL. Qualitatively, both structures are quite similar. The only noticeable difference is a higher level near the edge, for the case without the PNL. In conclusion, we can say from our simulation that the PNL has no relevant effect on both the structure of zonal flows and the radial transport for CYCLONE parameters.

ETG SIMULATIONS

Lately, there has been a growing interest in ETG turbulence, which, according to flux-tube simulations [2] could be experimentally relevant. On the other hand, global PIC ETG simulations [3] found a negligible transport level. To explain this large discrepancy, mainly two possible mechanisms have been invoked: a nonlinear toroidal coupling, which is not retained by flux-tube codes [3] and statistical noise induced by the PIC method [7]. Therefore, a quantification of numerical noise is desirable. The latter is created during the charge assignment, a process equivalent to a Monte-Carlo integra-

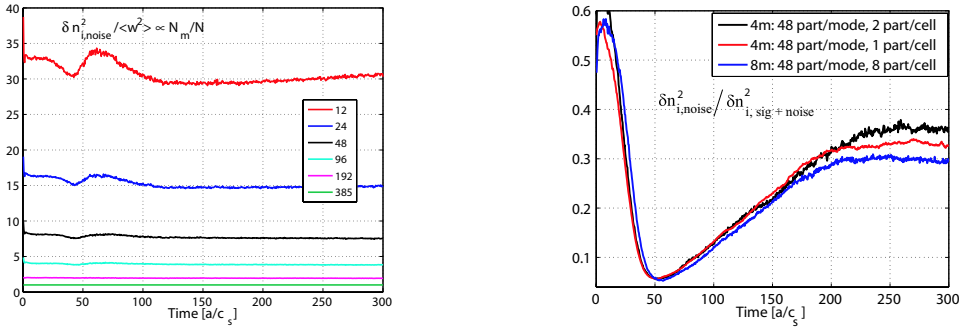

FIGURE 8. $\delta n_{i,\text{noise}}/\langle w^2\rangle$ for different values of N/N_m, normalized to the case with $N/N_m = 385$ (left) and noise to signal ratio for different numbers of markers per cell, but with constant number of markers per modes. These figures were published in [1]

tion [16]. According to [1], we have:

$$\delta n_i = \delta n_{i,\text{signal}} + \delta n_{i,\text{noise}}, \qquad \delta n_{i,\text{noise}} = \frac{N_m}{N}\langle w^2\rangle G \tag{26}$$

Where N_m is the number of Fourier modes in the simulation, N is the number of markers, $\langle w^2\rangle = 1/N\sum_{i=1}^{N} w_i^2$ and G is a factor which depends on the projection algorithm. Eq. (26) tells us how to decrease numerical noise: by increasing the number of markers, by reducing the number of Fourier modes in the simulation, by using sampling methods such as optimized loading [11] to reduce the statistical variance of the weights or to improve the projection algorithm, for example with higher order splines. In practice, $\delta n_{i,\text{noise}}$ is obtained by adding the contribution of filtered modes before the filtering process. To check the validity of Eq. (26), CYCLONE ETG simulations with $\rho_e^* = 1/80$ have been performed. In the left plot of Fig. 8, the value of $\delta n_{i,\text{noise}}/\langle w^2\rangle$ is displayed. We see that the noise is clearly proportional to N_m/N, demonstrating Eq. 26. The right plot of Fig. 8 shows that numerical noise does not depend on the number of markers per cell, but on the number of markers per mode. In order to quantify the radial transport for ETG turbulence, simulations have been performed with a more realistic $\rho_e^* = \frac{1}{450}$. The noise to signal ratio does not exceed 15%. Fig. 9 shows the temporal evolution of $\chi_e/\chi_{e,GB}$ vs $R_0/L_{T,e}$. Due to profile relaxation, the expected value for $\chi_e/\chi_{e,GB}$ can be estimated by a linear fit from the values obtained when the relaxation is small, i.e. at the end of the simulation. The fit indicates that $\chi_e/\chi_{e,GB} \cong 14$, which is in agreement with flux-tube simulations. To make more quantitative predictions and to recover the flux-tube limit, a smaller value of ρ_e^* is required, which is impossible with the computational power at our disposal.

CONCLUSIONS

Discrepancies obtained with the different existing gyrokinetic codes have emphasized the need to demonstrate the validity of PIC simulations. The trust in ORB5 simulations is obtained with excellent energy conservation and low numerical noise. The key algorithm is the field aligned Fourier filter, whose implementation is extremely simple and could

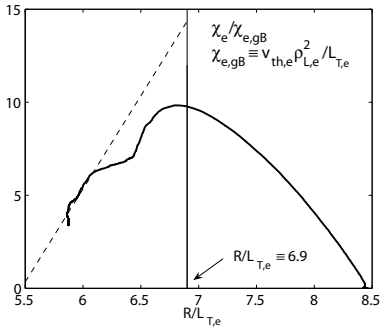

This figure was previously published in [1].

FIGURE 9. Temporal evolution of χ_e/χ_{GB} vs $R_0/L_{T,e}$ for a CYCLONE ETG simulation with $\rho^* = 1/450$.

be applied to any gyrokinetic code. The FAF reduces the number of Fourier modes by one order of magnitude and allows us to increase the time step by the same amount. In addition to a huge gain of CPU, the field-aligned filter enhances energy conservation and yields low numerical noise. Therefore, ORB5 is a powerful tool for studying ITG and ETG turbulence. Our simulations have shed light on 2 important topics in the gyrokinetic community. Firstly, there is no visible effects of the parallel nonlinearity on both the zonal flow structure and the radial transport for small ρ^* values, but this term should nevertheless be kept in the model to ensure energy and particle number conservation. Secondly, the new noise diagnostic implemented in ORB5 shows that the noise depends on the number of markers per Fourier mode kept in the filter. We could thus perform low-noise ETG CYCLONE simulation, whose transport level is comparable with flux-tube simulations.

ACKNOWLEDGMENTS

This research was partially sponsored by the Fonds National Suisse de la Recherche Scientifique and by Euratom. All simulations were performed on the IBM BlueGene Cluster of the Ecole Polytechnique Fédérale de Lausanne.

REFERENCES

1. A. Bottino, P. Angelino, R. Hatzky, S. Jolliet, A. G. Peeters, E. Poli, O. Sauter, T. M. Tran and L. Villard *Proc. 33rd EPS Conf. on Plasma Physics and Controlled Fusion (Roma, Italy, June 2006), to be published*.
2. F. Jenko and W. Dorland, *Phys. Rev. Lett.* **89**, 225001 (2002).
3. Z. Lin, L. Chen and F. Zonca *Phys. Plasmas* **12**, 056125 (2005).
4. L. Villard, P. Angelino, A. Bottino, S. J. Allfrey, R. Hatzky, Y. Idomura, O. Sauter and T. M. Tran *Plasma Phys. Controlled Fusion* **46**, B51 (2004).
5. J. Candy and R. E. Waltz *Phys. Plasmas* **13**, 032310 (2006).
6. T. M. Tran, K. Appert, M. Fivaz, G. Jost, J. Vaclavik and L. Villard *Theory of fusion Plasmas, Int. Workshop, Editrice Compositori, Societá italiana di Fisica, Bologna* p.45 (1999).
7. W. M. Nevins, G.W. Hammett, A.M. Dimits, W. Dorland and D.E. Shumaker *Phys. Plasmas* **12**, 122305 (2005).

8. T. S. Hahm *Phys. Fluids* **31**, 2670 (1988).
9. M. Kotschenreuther *Bull. Am. Phys. Soc.* **33**, 2107 (1988).
10. Y. Idomura, S. Tokuda and Y. Kishimoto *Nucl. Fusion* **43**, 234 (2003).
11. R. Hatzky, T. M. Tran, A. Könies, R. Kleiber and S. J. Allfrey *Phys. Plasmas* **9**, 898 (2002).
12. M. Fivaz, S. Brunner, G. de Ridder, O. Sauter, T. M. Tran, J. Vaclavik, L. Villard and K. Appert *Comp. Phys. Comm.* **111**, 27 (1998).
13. A. M. Dimits, G. Bateman, M. A. Beer, B. I. Cohen , W. Dorland, G. W. Hammet, C. Kim, J. E. Kinsey , M. Kotschenreuter, A. H. Kritz, L. L. Lao, J. Mandrekas, W. M. Nevins, S. E. Parker, A. J. Redd, D. E. Shumaker, R. Sydora and J. Weiland *Phys. Plasmas* **7**, 969 (2000).
14. S. Brunner PhD Thesis No.1701, Ecole Polytechnique Fédérale de Lausanne, 1997.
15. L. Villard, S. J. ALlfrey, A. Bottino, M. Brunetti, G. L. Falchetto, V. Grandgirard, R. Hatzky, J. Nührenberg, A. G. Peeters, O. Sauter, S. Sorge and J. Vaclavik *Nucl. Fusion* **44**, 172 (2004).
16. A. Y. Aydemir *Phys. Plasmas* **1**, 822 (1994).